

<https://doi.org/10.1038/s41528-024-00304-4>

Flexible and wearable battery-free backscatter wireless communication system for colour imaging

Check for updates

Jun-Lin Zhan^{1,2}, Wei-Bing Lu^{1,2}✉, Cong Ding^{1,2}, Zhen Sun^{1,2}, Bu-Yun Yu^{1,2}, Lu Ju^{1,2}, Xin-Hua Liang³, Zhao-Min Chen^{1,2}, Hao Chen^{1,2}, Yong-Hao Jia^{1,2}, Zhen-Guo Liu^{1,2} & Tie-Jun Cui¹✉

Wireless imaging, equipped with ultralow power wireless communications and energy harvesting (EH) capabilities, have emerged as battery-free and sustainable solutions. However, the challenge of implementing wireless colour imaging in wearable applications remains, primarily due to high power demands and the need to balance energy harvesting efficiency with device compactness. To address these issues, we propose a flexible and wearable battery-free backscatter wireless communication system specially designed for colour imaging. The system features a hybrid RF-solar EH array that efficiently harvests energy from both ambient RF and visible light energy, ensuring continuous operation in diverse environments. Moreover, flexible materials allow the working system to conform to the human body, ensuring comfort, user-friendliness, and safety. Furthermore, a compact design utilizing a shared-aperture antenna array for simultaneous wireless information and power transfer (SWIPT), coupled with an optically transparent stacked structure. This design not only optimizes space but also maintains the performance of both communication and EH processes. The proposed flexible and wearable systems for colour imaging would have potentially applications in environmental monitoring, object detection, and law enforcement recording. This approach demonstrates a sustainable and practical solution for the next generation of wearable, power-demanding devices.

Backscatter communication, characterized by its low-power and low-cost features, plays a crucial role in managing the increasing power consumption of wirelessly connected devices in Internet of things (IoT) systems¹. The development of flexible backscatter communication devices and systems, using additive manufacturing and inkjet printing, has opened up possibilities for applications in body sensor networks (BSNs)^{2–5}. The integration of backscatter communication with energy harvesting (EH) techniques enables battery-free operations, a crucial step towards sustainable device development. Due to the typically lower sensitivity and efficiency of radio frequency (RF) EH compared to wireless communication⁶, integrating additional energy sources into EH systems has attracted significant interests^{7–12}. Imaging technologies, central to applications like environmental monitoring, object detection, and law enforcement^{13–18}, have notably advanced through the integration of backscatter communication and EH^{9–11}, leading to the development of battery-free wireless grayscale imaging solutions. However, implementing wireless color imaging in wearable

devices poses challenges. Compared to grayscale, the primary issue is the higher power requirement of color imaging¹⁹, which complicates the already challenging task of balancing power density with the compactness needed for wearable applications.

RF, ambient light, thermoelectric and biomechanical energy sources are increasingly sought-after in wearable battery-free applications¹². While hybrid RF-solar EH is promising^{9,20}, its compact integration with backscatter communication for wearable is challenging. Advancements in transparent stacked hybrid RF-solar EH, using transparent materials, have enabled complete solar cell utilization²¹. Additionally, antenna multiplexing techniques such as polarization splitting²², power splitting²³, and frequency splitting (FS)^{24,25} are increasingly employed for simultaneous wireless information and power transfer (SWIPT)^{22–26}. The use of a shared aperture design allows antennas operating at different frequencies to coexist in a compact space, optimizing space utilization²⁷. Moreover, in wearable applications, addressing the specific absorption rate (SAR) is crucial. Thus,

¹State Key Laboratory of Millimeter Waves, School of Information Science and Engineering, Southeast University, Nanjing 210096, China. ²Center for Flexible RF Technology, Frontiers Science Center for Mobile Information Communication and Security, Southeast University, Nanjing 210096, China. ³College of Electronic and Information Engineering, Nanjing University of Aeronautics and Astronautics, Nanjing 211106, China. ✉e-mail: wblu@seu.edu.cn; tjcui@seu.edu.cn

implementing shielding between antennas and the human body is an effective strategy to reduce SAR exposure²⁸.

Here, we propose a flexible and wearable battery-free backscatter wireless communication system tailored for colour imaging. The system incorporates a hybrid RF-solar EH array that enhances EH from ambient RF signals and visible lights, overcoming the limitations of conventional approaches. The hybrid EH array significantly boosts energy harvesting, facilitating ultra-low power backscatter communication and effective power management for both outdoor and indoor usage. Additionally, flexibility is achieved through the use of flexible conductors and substrates, allowing the system to operate after conforming to the human body, thus ensuring comfort, user-friendliness, and safety due to minimized specific absorption rates (SAR). The system also exhibits stable off-body communication performance, a benefit stemming from its radar cross-section (RCS) being minimally affected by modulation states. Furthermore, a compact form is achieved through the FS-SWIPT technique and a transparent stacked hybrid RF-solar EH array. The FS-SWIPT approach facilitates the concurrent functioning of RF EH and backscatter communication through a shared-aperture antenna array, effectively reducing interference between these operations. And the optically transparent stacked structure not only maintains both RF and solar EH efficiency but also ensures that the performance of RF components remains unaffected by the presence of solar cells. The innovative strategies employed address critical challenges in power generation, system flexibility, and compactness, demonstrating a sustainable and practical solution for the next generation of wearable and power-demanding devices.

Results and Discussion

Flexible battery-free communication system

Figure 1 illustrates the compact, flexible, and battery-free backscatter communication system designed for wearable wireless colour image capture. The system, covering an area of 400 cm², comprises a transparent FS-SWIPT device, a hybrid RF-solar EH array, a flexible printed circuit (FPC) with a camera (CAM), a PMU, and a microcontroller

(MCU). The transparent FS-SWIPT device, placed on top of the solar cells and FPC, uses a shared-aperture-type design to obtain RF signals for backscatter modulation and rectification at 3.5 GHz and 2.4 GHz, respectively. The patch-type FS-SWIPT device is chosen to mitigate the impact of human body influences, while the transparent conductor in FS-SWIPT device shields it from solar cells and the FPC. To ensure a stable connection, the RF switch and rectifier in the FS-SWIPT device are connected with transparent microstrip lines via a combination of conductive ink and solder paste. The solar cells are connected in series with the rectenna array for large-area hybrid RF-solar EH, with the solar cells covering 80% of the entire area. The PMU is responsible for energy storage and output stability. Once sufficient energy is generated, colour images are captured and coded by CAM and MCU. Then the modulator in the FS-SWIPT device is controlled by the MCU for backscatter communication. Figure 2c demonstrates the system's flexibility, showcasing its ability to conform to a cylindrical shape.

Figure 2a demonstrates the system's indoor and outdoor communication prototypes, highlighting its compactness and flexibility when mounted on clothing, with an USRP LW-N310 configured for 3.5 GHz backscatter communication and a 2.4 GHz RF source. During indoor testing, after being fully charged by light and RF energy, the system captures one color image at a resolution of 100 × 100 pixels via the CAM. The captured image is then transmitted to the USRP for display and storage through backscatter communication (Supplementary Movie 1). In outdoor scenarios, the hybrid RF-solar EH array consistently powers the power under direct sunlight. The tests confirm a communication distance of 25 cm and a data rate of 500 kbps (detailed in Supplementary Note 4). Figure 2b illustrates SAR simulations for backscatter communication, with a 38 dBm equivalent isotropic radiation power (EIRP) RF source positioned 25 cm from the system. The maximum SAR values are 0.50 W kg⁻¹ and 0.66 W kg⁻¹ at 2.4 GHz and 3.5 GHz, respectively, which are lower than the standard value of 1.6 W kg⁻¹ regulated by the Federal Communications Commission (FCC)²⁹. Figure 2d and Supplementary Figure 8c-e illustrate

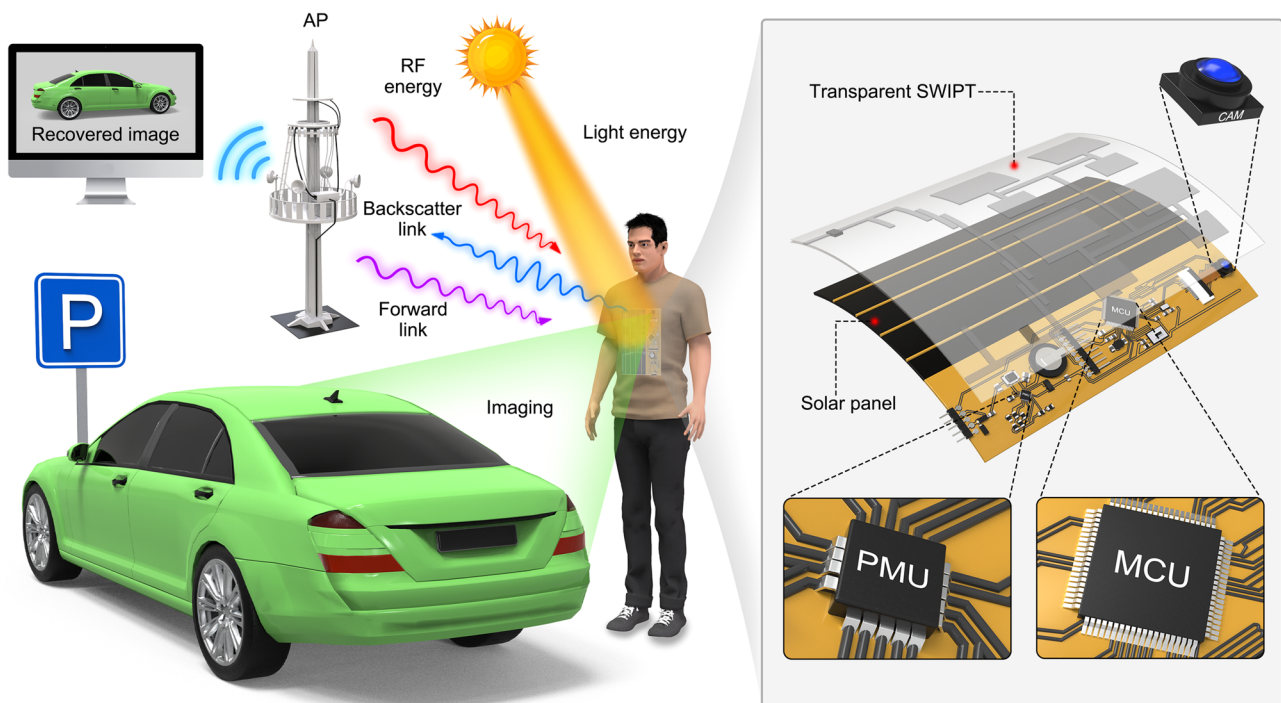


Fig. 1 | Highly compact flexible and battery-free backscatter communication system for wearable wireless imaging. The system consists of a transparent SWIPT device, solar cells, a PMU, an MCU, and a CAM. When equipped on the chest and

next to an access point (AP), it captures and transmits the image back to the AP for display after harvesting sufficient RF and light energy.

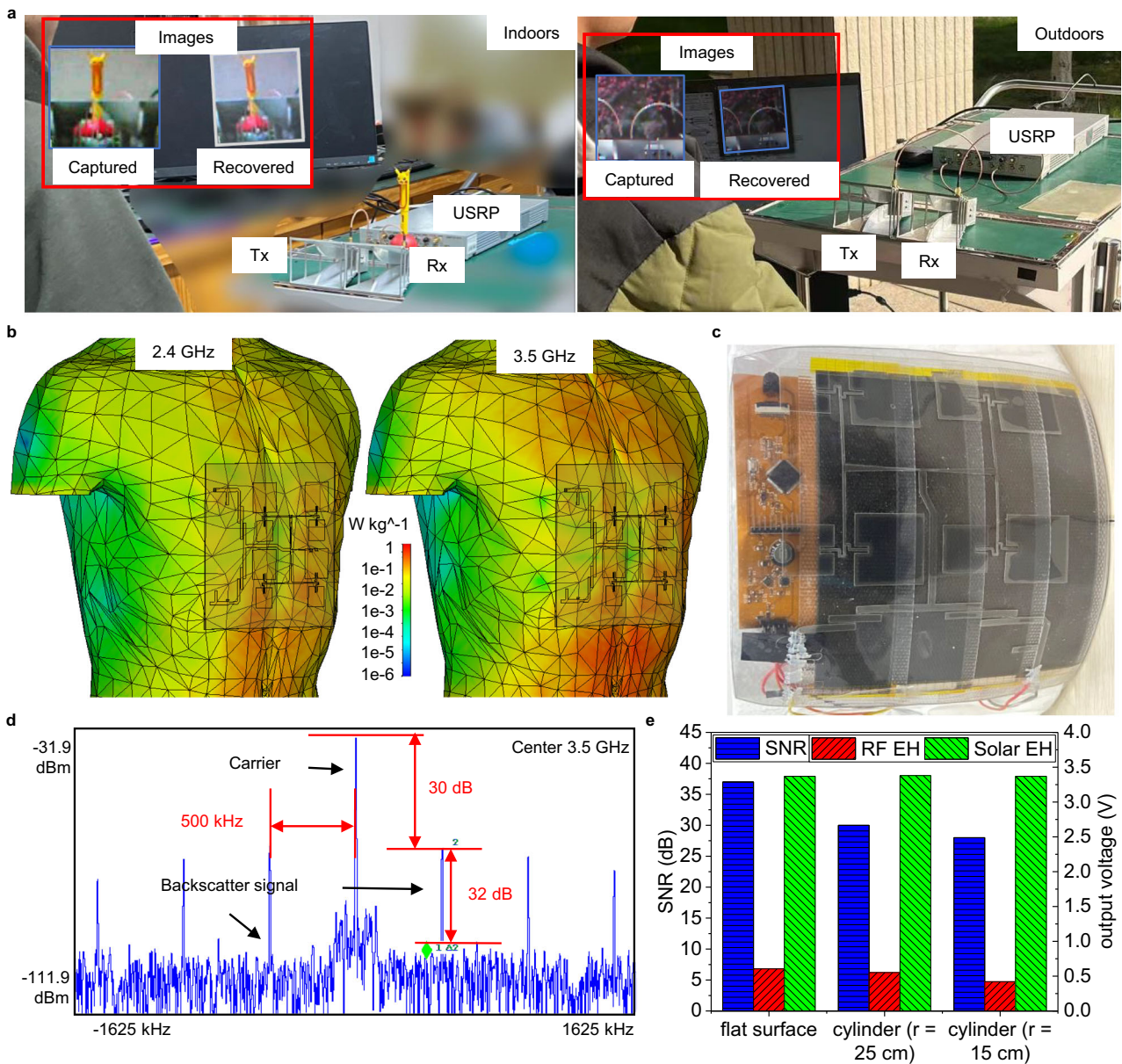


Fig. 2 | Proposed flexible and battery-free system for wearable wireless imaging. a On-body communication prototype indoors and outdoors. b SAR simulation at 2.4 GHz (left) and 3.5 GHz (right) in backscatter communication. c Photograph of

the flexible system bent on a cylinder with 15 cm radius. d Spectrum in backscatter communication. e Performances of backscatter communication, RF and solar EH.

the backscatter communication performance using binary phase-shift keying (BPSK) modulation at 3.5 GHz. The communication achieves a carrier-to-noise ratio (CNR) of 62 dB. Additionally, the backscatter signals, 500 kHz from the carrier, exhibit a signal-to-noise ratio (SNR) of 32 dB. The modulator power consumption is below 6.6 mW³⁰, whereas the operating CAM and MCU consume approximately 100 mW, as tested with the RIGOL programmable DC power supply DP831. Additional experimental data (Supplementary Fig. 8f) with a 27 dBm EIRP RF source investigate the relationship between communication distance and data rate. Data rate is set at levels above 100 kbps, considering the increased noise levels in the USRP within 100 kHz bandwidth, as depicted in Fig. 2d. It reveals that at a data rate of 125 kbps, the system achieves its maximum communication distance of 250 cm. When the data rate is lower to 100 kbps, the distance is reduced, which is attributed to the higher noise levels in the USRP.

To determine bending effects on the performance in energy harvesting and backscatter communication, we conducted

experiments with the flexible system attached to flat surface and cylinders with radii of 25 cm (Supplementary Fig. 11b) and 15 cm (Supplementary Fig. 11c). In Fig. 2e, the blue and red columns represent the experimental SNR in backscatter communication (at a data rate of 500 kbps) and the output voltage of RF EH, respectively. These were measured using a 27 dBm EIRP RF source, placed 25 cm from the system. The results indicate a slight decrease in both backscatter communication and RF EH performance as the degree of bending increases, attributed to the antenna array's radiation deterioration. The green column shows the solar EH output voltage under approximately 8000 lux the light intensity on the solar cell array, demonstrating stable performance despite varying degrees of bending.

Transparent FS-SWIPT device

Figure 3a depicts a schematic of the FS-SWIPT device, The solid line represents the forward link channel at frequency f_B and RF energy at f_R .

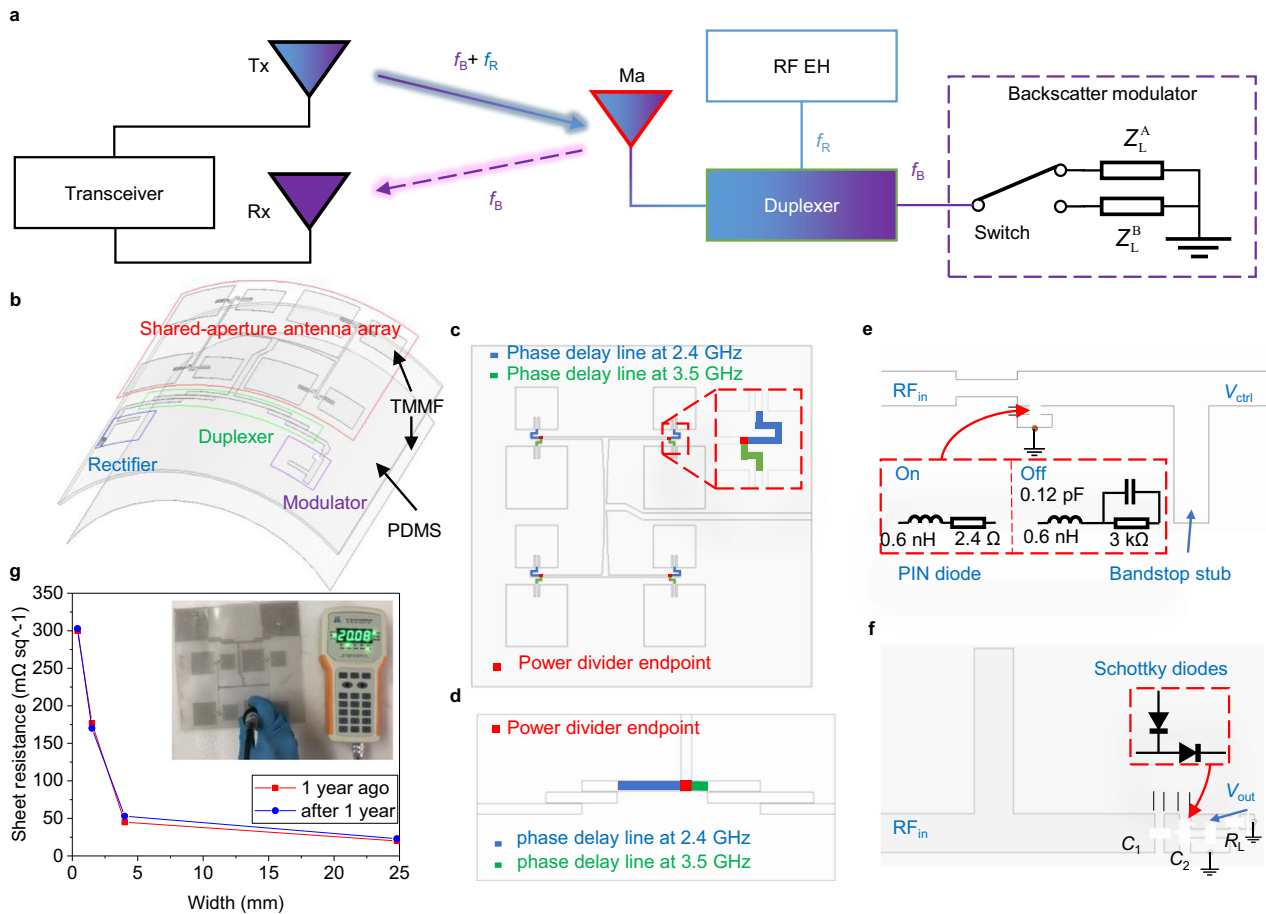


Fig. 3 | Transparent SWIPT device. **a** Schematic of the FS-SWIPT device. **b**, Exploded diagram of the flexible type of device. **c**, Dual-band shared-aperture antenna array. **d** Duplexer. **e** Modulator. **f** Rectifier, where $C_1 = 10$ pF, $C_2 = 100$ pF, and $R_L = 1$ kΩ. **g** Measured sheet resistances of the TMMF in different widths over a duration of one year.

emitting from the transmitting antenna to the terminal antenna. The dotted line denotes the backscatter link channel at f_B , reflected from the terminal antenna to the receiving antenna. The duplexer splits the forward link channel and RF energy for backscatter modulation and RF EH, respectively. The forward and backscatter link budgets are defined as follows³¹:

$$P_M = \frac{P_T G_T G_M \lambda^2 X_f}{(4\pi r_f)^2 \Theta B_f F_f} \quad (1)$$

$$P_R = \frac{P_T G_T G_R G_M^2 \lambda^4 X_f X_b M}{(4\pi)^4 r_f^2 r_b^2 \Theta^2 B_f B_b F_b} \quad (2)$$

where λ is the wavelength; Θ is the on-object antenna gain penalty; P_T , P_M , and P_R are the transmitter transmitting power, modulator power and receiver receiving power, respectively; G_T , G_M , and G_R are the gains of the transmitting antenna, modulator antenna, and receiving antenna, respectively; r_f and r_b are the distances of the forward and backscatter links, respectively; X_f and X_b are the forward and backscatter polarization mismatches, respectively; B_f and B_b are the forward and backscatter path-blockage losses, respectively; F_f and F_b are the forward and backscatter fade margins, respectively. The modulation factor M is determined by the modulator reflection coefficients Γ_A and Γ_B in different states³²:

$$M = \frac{1}{4} |\Gamma_A - \Gamma_B|^2 \quad (3)$$

$$\Gamma_A = \frac{Z_L^A - Z_A^*}{Z_L^A + Z_A} \quad (4)$$

$$\Gamma_B = \frac{Z_L^B - Z_A^*}{Z_L^B + Z_A} \quad (5)$$

where Z_A is the modulator antenna impedance, and Z_L^A and Z_L^B are the load impedances in different states.

The transparent FS-SWIPT device, detailed in Fig. 3b–f, incorporates a dual-band shared-aperture antenna array with a duplexer, modulator, and rectifier. Constructed using transparent micromeshed metal film (TMMF) and polydimethylsiloxane (PDMS) for the conductor and substrate, respectively, the device’s detailed parameters are provided in Supplementary Figure 10. Comparisons between substrates of varying thicknesses are explored in Supplementary Note 3 and Supplementary Fig. 5. Stability tests of the TMMF’s sheet resistances over a year, depicted in Fig. 3g, confirm their consistency, underlining the system’s reliability for long-term use.

The electromagnetic (EM) waves in the dual-band shared-aperture antenna array (Figs. 3c, 4c), operating at 2.4 GHz and 3.5 GHz, are divided by a 1:4 power divider. At the endpoints (red points in Fig. 3c), the lengths of the phase delay lines (blue and green lines in Fig. 3c) are adjusted to minimize interference between adjacent antennas at different frequencies (detailed in Supplementary Note 3 and Supplementary Fig. 4). The far field of the antenna array is measured in an anechoic chamber (Fig. 4a), and the simulated and measured results of the antenna array are presented in Fig. 4b, c. The results show that the reflected wave is in-phase with the input wave at the endpoint of the antenna unit (Fig. 4c) when the length of the

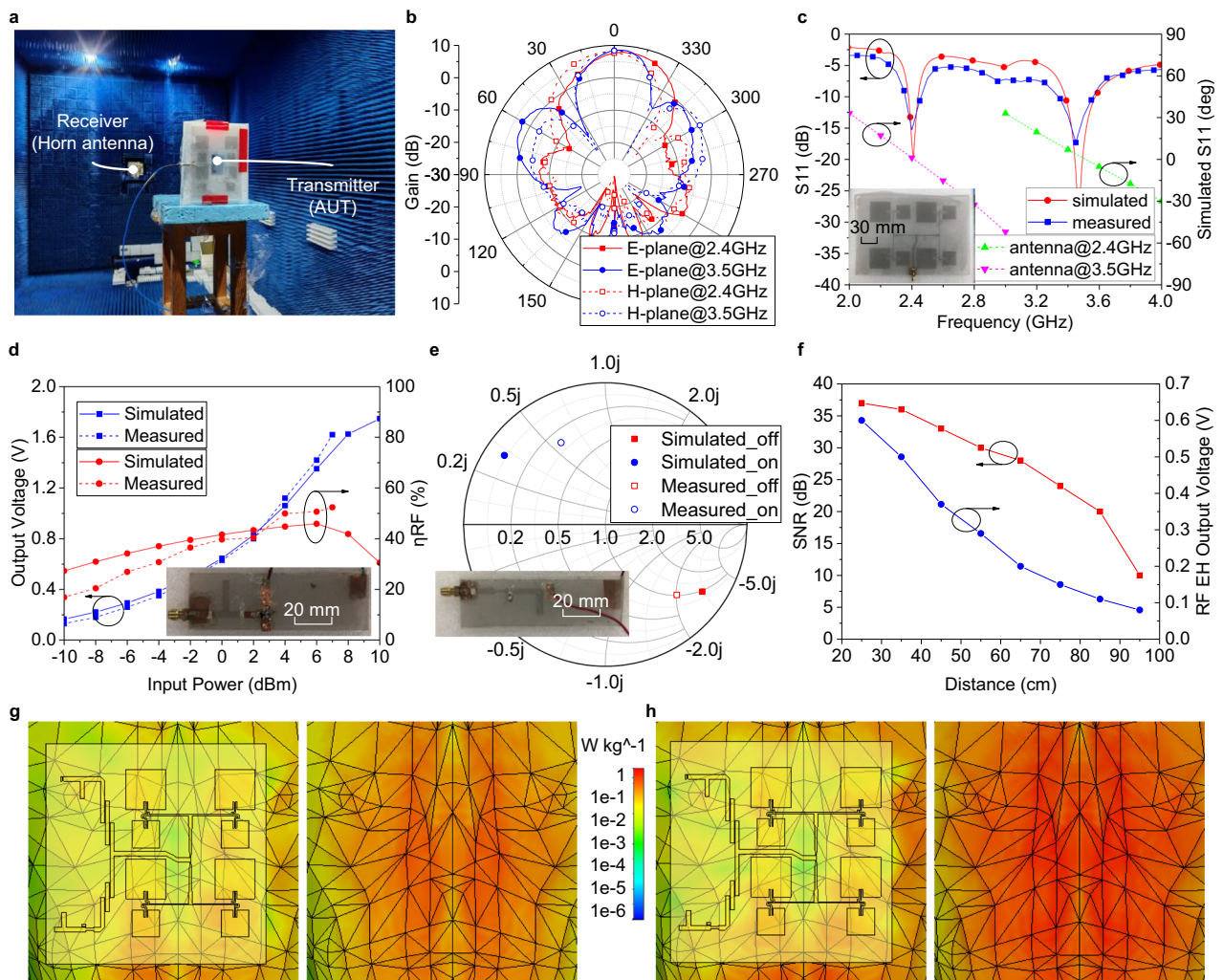


Fig. 4 | Simulated and measured results for the transparent FS-SWIPT device. **a** Photograph of the far-field experimental setup. **b, c** Results of the dual-band shared-aperture antenna array: measured radiation patterns at 2.4 GHz and 3.5 GHz (**b**), and S_{11} (**c**), where the scale bar is 30 mm. **d** Output voltage, and rectification efficiency of the rectifier, where the scale bar is 20 mm. **e** S-parameters of the

modulator in different states, where the scale bar is 20 mm. **f** Relationship between the distance of the USRP device and the system's energy harvesting and backscatter communication. **g** SAR simulation with and without the FS-SWIPT device at 2.4 GHz. **h** SAR simulation with and without the FS-SWIPT device at 3.5 GHz.

phase delay lines is adjusted to 7.5 mm and 14 mm at 2.4 GHz and 3.5 GHz, respectively. This confirms that the proposed antenna array is well-matched at both frequencies. The gains are 7.7 dBi at 2.4 GHz and 8.4 dBi at 3.5 GHz (Fig. 4b and Supplementary Fig. 4), but the sidelobe is high at 3.5 GHz due to the same distance p between adjacent antennas at different frequencies (0.648 of the wavelength at 2.4 GHz, 0.945 of the wavelength at 3.5 GHz). The SAR of the antenna array is discussed in Supplementary Note 3 and Supplementary Fig. 4.

Upon reception by the antenna array, the EM waves are directed to the duplexer (Fig. 3d and Supplementary Fig. 5d), which separates them into the rectifier and modulator. The duplexer is composed of two 1st-order coupled-line bandpass filters, and the lengths of the phase delay lines are adjusted to minimize interference between the filters. The simulated and measured results of the duplexer are presented in Supplementary Fig. 5. At 2.4 GHz and 3.5 GHz, the duplexer insertion loss measures 2.4 dB and 2.7 dB, respectively, while the isolation between the two outputs is approximately 25 dB.

The RF switch (Figs. 3e, 4e) is responsible for modulating RF signals at 3.5 GHz using BPSK modulation. To prevent RF signals from reaching the control port, a bandstop stub is included (detailed in Supplementary Note 3). Both conductive ink and solder paste are used to connect the RF switch and microstrip lines (Fig. 6b and Supplementary Fig. 3). The simulated and measured results of the modulator are presented in Fig. 4e and

Supplementary Fig. 6a, b. The modulator displays a phase difference of approximately 160° and has a 3 dB return loss in the on/off states at 3.5 GHz. The modulation factor M is calculated as 0.45 as per Eq. (3).

The rectifier (Figs. 3f, 4d) is responsible for converting RF energy at 2.4 GHz to DC energy and storing it in the PMU. The soldering process for the Schottky diodes and capacitors is the same as that used for the RF switch above. The simulated and measured results of the proposed rectifier are displayed in Fig. 4d and Supplementary Fig. 6c. The rectifier output voltage evidently ranges from 0.17 V to 1.7 V when the input power increases from -10 dBm to +10 dBm. However, power management chips often have cold-start voltages that cannot be achieved with weak RF energy alone. Therefore, hybrid RF-solar EH, which combines RF energy with light energy, is currently a high-priority research topic.

To study the performance of the FS-SWIPT device in wearable battery-free communication, a linearly polarized wave is radiated on the FS-SWIPT device to observe the induced currents and scattered patterns, as shown in Supplementary Fig. 7. The magnitudes of the induced currents and normalized radar cross-section (RCS) patterns are relatively insensitive to the state of the modulator. The induced currents flow into the modulator and rectifier at frequencies of 3.5 GHz and 2.4 GHz, respectively (Supplementary Fig. 7a, b). Additionally, the sidelobe levels (SLL) in RCS patterns are observed to be above 10 dB in Supplementary Fig. 7c. When the FS-SWIPT

device is attached on the human body, the RCS patterns are approximately unchanged (Supplementary Fig. 7c). Meanwhile, the SAR reduces apparently within the range of the FS-SWIPT device, compared with the SAR without the device (Fig. 4g, h). Additionally, we conducted experiments on the relationship between the USRP device distance and the FS-SWIPT device performance, using a 27 dBm EIRP RF source and setting the data rate to 500 kbps. Figure 4f describes a decrease in SNR and RF EH output voltage with increasing distance, due to RF energy dissipation.

Hybrid RF-solar EH array

The hybrid RF-solar EH array is shown in Fig. 5a, which consists of both RF EH and solar EH. To achieve a high energy conversion efficiency, a single stub is used to match the RF-EH output in Fig. 5a to the rectified diodes. The RF energy is then converted to DC energy E_1 through full-wave rectification. Capacitors C_1 and C_2 are used for DC blocking and bypass, respectively. Solar cells are used to convert light energy to DC energy E_2 , with a maximum output power of 2 W outdoors. Zener diodes D_1 and D_2 are used to prevent overloaded voltage and reverse current, respectively. Both E_1 and E_2 are managed and stored in supercapacitor C_3 by the PMU to activate the load. The RF-to-DC conversion efficiency η_{RF} can be calculated using³³:

$$\eta_{RF} = \frac{P_{out}}{P_{in}^{RF} | P_{in}^{Solar} = 0} \times 100\% \quad (6)$$

$$P_{out} = \frac{V_{out}^2}{R_L} \quad (7)$$

where P_{in}^{RF} and P_{in}^{Solar} are the RF and solar input power, respectively, and V_{out} and P_{out} are the voltage and power across load R_L , respectively. In Fig. 4f, the conversion efficiency η_{RF} of the rectifier ranges between 27% and 46%.

The RF EH test scenario and output voltages of the hybrid RF-solar EH array and PMU under different light and RF intensities are shown in Fig. 5b and c. The results demonstrate that the performance of the hybrid RF-solar EH array is influenced by both light intensity and EIRP. Notably, the PMU maintains a stable output across these varying conditions. It is capable of functioning efficiently at a light intensity as low as 13 lux or with an EIRP input of 27 dBm from a distance of 25 cm.

To comprehensively evaluate the hybrid RF-solar EH array, we investigated the directionality effects on its energy harvesting capabilities, with findings presented in Fig. 5d. Using a 27 dBm EIRP horn antenna placed 25 cm from the system, we measured the RF EH output voltage across various incident angles. This data, shown as the red line, correlates with the radiation pattern in Fig. 4b, revealing a minimum RF EH output voltage at a 60° incident angle. Additionally, the solar EH output voltage, depicted by the blue line, was assessed using a light source emitting around 8000 lux at vertical incidence on the surface of the solar cell array. Here, the solar EH output voltage decreases as the incident angle increases, a trend explained by the diminishing light intensity on the system's surface.

Discussion

We have successfully developed and demonstrated a flexible and wearable battery-free backscatter wireless communication system for colour imaging. The system incorporates several innovative features and achieves significant advancements in performance. One key aspect is the integration of a hybrid RF-solar EH array, which efficiently harvests energy from both ambient RF signal and visible light, ensuring sustainable and reliable energy sources. Experiments enrich the understanding of the EH array's performance under various environmental conditions. Additionally, the use of flexible materials enhances its wearability and comfort. We have demonstrated through off-body simulations that the system effectively reduces the SAR and maintains a stable RCS. Experiments evaluate the robustness of the system under different bending scenarios. Furthermore, the stacked and shared-aperture design achieves the balance between energy-harvesting power density and device compactness. Finally, the off-body communication prototype demonstrates the battery-free system's potential in wearable wireless colour imaging.

There are several limitations that offer opportunities for future research. First, the hybrid RF-solar EH, especially under conditions of low light and RF energy, presents a challenge for power-hungry applications. Future versions could incorporate diverse types of EH to bolster energy intake under various environmental conditions. Second, the current data transmission rate and resolution of color imaging, while adequate for certain applications, may not meet the demands of more advanced or high-resolution imaging tasks. Potentially integrating machine learning algorithms, such as NeuriCam¹⁹, this system can further reduce power consumption and facilitate color video transmission, expanding the system's

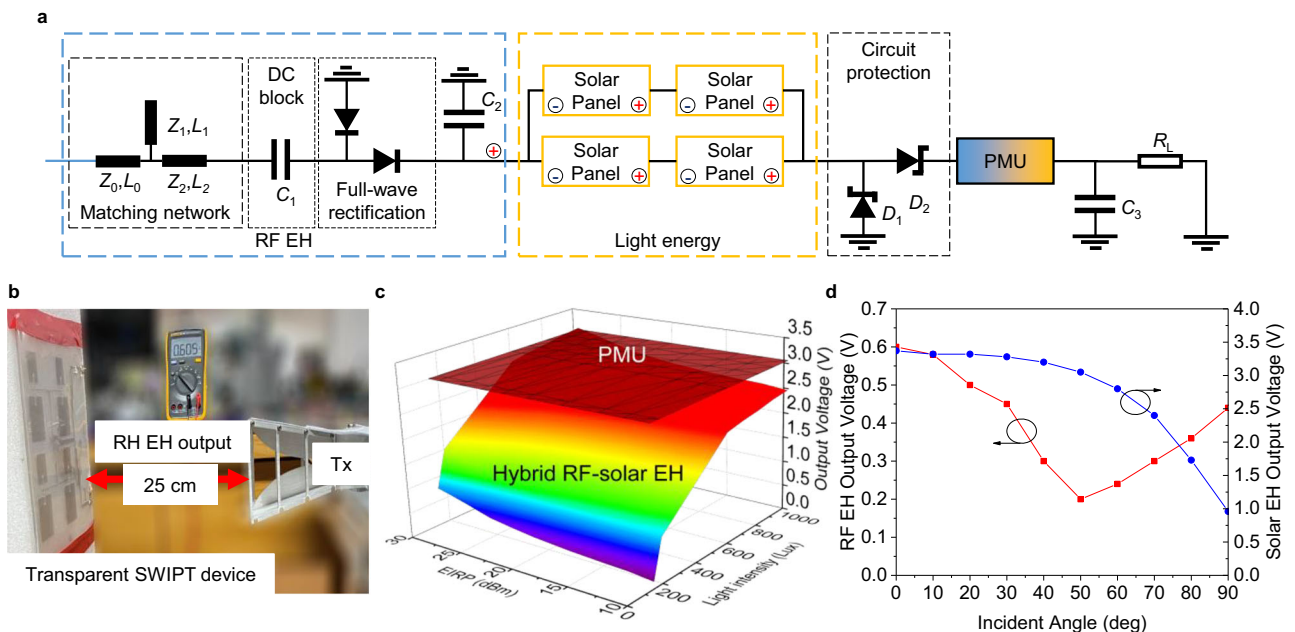


Fig. 5 | Hybrid RF-solar EH. **a** Schematic. **b** RF EH test scenario. **c** Output voltages of the hybrid RF-solar EH array and the PMU under different light and RF intensities. **d** Energy harvesting capabilities with respect to different directions of light and electromagnetic waves.

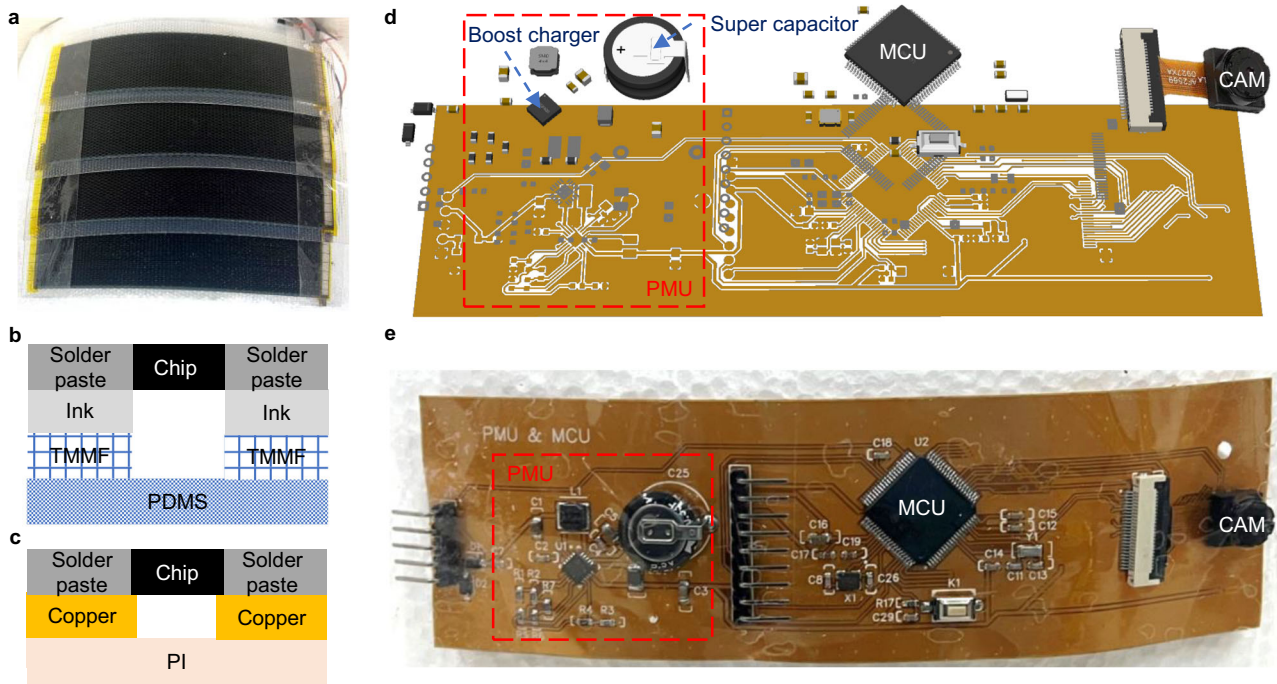


Fig. 6 | Structure of the flexible solar cell array and circuit board. a Photograph of the connected flexible solar cell array bent on a cylinder with 15 cm radius. **b** Component connection in the transparent SWIPT device. **c** Components connection in the FPC. **d** Exploded diagram of the flexible circuit board with PMU, MCU, and CAM. **e** Photograph of the flexible circuit board bent on the cylinder.

capabilities. Third, the envisioned integration with existing wireless networks and IoT devices requires a more in-depth exploration. Future research should focus on seamless interoperability with current communication protocols and standards, like BackFi³⁴, to ensure easy adaptability of the system within the rapidly evolving tech landscape.

Methods

Flexible and transparent materials

The flexible and transparent FS-SWIPT device is fabricated using PDMS as the substrate ($\epsilon_r = 2.8$, $\tan \delta = 0.02$, 1.5 mm thick), involving a process of mixing, stirring, confining, expelling, and thermal curing³⁵, as detailed in Supplementary Note 1. The conductor TMMF with a sheet resistance of $\leq 0.09 \Omega \text{ sq}^{-1}$ and a thickness of 150 μm , is adhered to the substrate and shaped using laser cutting³⁶, with further details in Supplementary Note 2.

Modulation

For the RF switch, we employed a BAR64-02V PIN diode from Infineon³⁷, controlled by the Microcontroller Unit (MCU), as shown in Fig. 3e. The PIN diode’s behavior, alternating between inductance with low resistance at a high control voltage ($V_{\text{ctrl}} = 0.8 \text{ V}$) and inductance with parallel high resistance and capacitance at a low control voltage ($V_{\text{ctrl}} = 0 \text{ V}$), enables variable RF switch states.

Energy harvesting

The rectifier employs two SMS7630 Schottky diodes from Skyworks for full-wave rectification³⁸ (Fig. 3f). These diodes are sensitive to -60 dBm of RF energy, though the PMU necessitates a higher input power for activation. The system’s flexible solar cell array (Fig. 6a) consists of four panels with an a-Si/a-SiGe/a-SiGe triple-junction structure ($V_{\text{oc}} = 2.2 \text{ V}$, $V_m = 1.6 \text{ V}$, $P_m = 0.5 \text{ W}$), as shown in Supplementary Figure 11a³⁹.

Flexible circuits

The design of the circuit board with Flexible Printed Circuit (FPC) techniques (Fig. 6d, e), incorporating PMU, MCU and CAM, achieves flexibility through a layout where rigid chips occupy only a small portion of the board. All components are soldered onto the FPC with solder paste (Fig. 6c), with

their schematics and detailed descriptions provided in Supplementary Note 5.

Data availability

All data needed to evaluate the conclusions in the paper are present in the paper and/or supplemental information. Additional data or code related to this paper are available from the corresponding author upon reasonable request.

Received: 13 July 2023; Accepted: 6 March 2024;

Published online: 14 March 2024

References

1. Memon, M. L., Saxena, N., Roy, A. & Shin, D. R. Backscatter Communications: Inception of the Battery-Free Era-A Comprehensive Survey. *Electronics* **8**, 129 (2019).
2. Eid, A. et al. Inkjet-/3D-/4D-printed perpetual electronics and modules: RF and mm-wave devices for 5G+, IoT, smart agriculture, and smart cities applications. *IEEE Microw. Mag.* **21**, 87–103 (2020).
3. Song, C. et al. Advances in Wirelessly Powered Backscatter Communications: From Antenna/RF Circuitry Design to Printed Flexible Electronics. *Proc. IEEE* **110**, 171–192 (2022).
4. Kimionis, J., Georgiadis, A., Daskalakis, S. N. & Tentzeris, M. M. A printed millimetre-wave modulator and antenna array for backscatter communications at gigabit data rates. *Nat. Electron.* **4**, 439–446 (2021).
5. Lin, T. H. et al. On-Body Long-Range Wireless Backscattering Sensing System Using Inkjet-/3-D-Printed Flexible Ambient RF Energy Harvesters Capable of Simultaneous DC and Harmonics Generation. *IEEE Trans. Microw. Theory Tech.* **65**, 5389–5400 (2017).
6. Talla, V., Smith, J., Gollakota, S. J. G. M. C. & Communications. Advances and Open Problems in Backscatter Networking. *GetMobile: Mob. Comp. Comm.* **24**, 32–38 (2021).
7. Eid, A., Hester, J. G., Tentzeris, M. M. J. I. A. & Letters, W. P. Rotman lens-based wide angular coverage and high-gain semipassive

- architecture for ultralong range mm-wave rfids. *IEEE Antennas Wirel. Propag. Lett.* **19**, 1943–1947 (2020).
8. Naderiparizi, S., Kapetanovic, Z. & Smith, J. R. Battery-Free Connected Machine Vision with WISPCam. *GetMobile: Mob. Comp. Comm.* **20**, 10–13 (2016).
 9. Saffari, A., Hessar, M., Naderiparizi, S. & Smith, J. R. Battery-Free Wireless Video Streaming Camera System. in *IEEE Int. Conf. Rfid* 1–8 (2019).
 10. Saffari, A. et al. Battery-Free Camera Occupancy Detection System. in *Proceedings of the 5th International Workshop on Embedded and Mobile Deep Learning* 13–18 (2021).
 11. Afzal, S. S. et al. Battery-free wireless imaging of underwater environments. *Nat. Commun.* **13**, 5546 (2022).
 12. Chong, Y. W., Ismail, W., Ko, K. & Lee, C. Y. Energy Harvesting For Wearable Devices: A Review. *Ieee Sens J.* **19**, 9047–9062 (2019).
 13. Healey, J. & Picard, R. W. StartleCam: A cybernetic wearable camera. *Second International Symposium on Wearable Computers - Digest of Papers*, 42–49 (1998).
 14. Castle, R. O., Klein, G. & Murray, D. W. Combining monoSLAM with object recognition for scene augmentation using a wearable camera. *Image Vis. Comput* **28**, 1548–1556 (2010).
 15. Anvesha, A., Xu, S. J., Cao, N. Y., Romberg, J. & Raychowdhury, A. A Light-powered, “Always-On”, Smart Camera with Compressed Domain Gesture Detection. in *Proceedings of the 2016 International Symposium on Low Power Electronics and Design* 118–123 (2016).
 16. Desai, S. J., Shoaib, M. & Raychowdhury, A. An Ultra-Low Power, “Always-On” Camera Front-End for Posture Detection in Body Worn Cameras Using Restricted Boltzman Machines. *IEEE Trans. Multi-Scale Comput. Syst.* **1**, 187–194 (2015).
 17. Mann, S. Wearable computing: A first step toward personal imaging. *Computer* **30**, 25–31 (1997).
 18. Silbergliitt, R., Lauland, A., Watson, M., Eusebi, C. A. & Lastunen, J. Wearable Technologies for Law Enforcement: Multifunctional Vest System Options. <https://doi.org/10.7249/RR2012> (RAND Corporation, 2017).
 19. Veluri, B. et al. NeuriCam: Key-Frame Video Super-Resolution and Colorization for IoT Cameras. in *Proceedings of the 29th Annual International Conference on Mobile Computing and Networking* 26 (2023).
 20. Bito, J. et al. A Novel Solar and Electromagnetic Energy Harvesting System With a 3-D Printed Package for Energy Efficient Internet-of-Things Wireless Sensors. *IEEE Trans. Microw. Theory Tech.* **65**, 1831–1842 (2017).
 21. Yu, B. Y. et al. Flexible and Wearable Hybrid RF and Solar Energy Harvesting System. *IEEE Trans. Antennas Propag.* **30**, 2223–2233 (2021).
 22. Lu, P., Song, C. Y. & Huang, K. M. A Two-Port Multipolarization Rectenna With Orthogonal Hybrid Coupler for Simultaneous Wireless Information and Power Transfer (SWIPT). *IEEE Trans. Antennas Propag.* **68**, 6893–6905 (2020).
 23. Lu, P., Huang, K. M., Song, C., Ding, Y. & Goussetis, G. Optimal Power Splitting of Wireless Information and Power Transmission using a Novel Dual-Channel Rectenna. *IEEE Trans. Antennas Propag.* **70**, 1846–1856 (2021).
 24. Correia, R., Carvalho, N. B. & Kawasaki, S. Continuously Power Delivering for Passive Backscatter Wireless Sensor Networks. *IEEE Trans. Microw. Theory Tech.* **64**, 3723–3731 (2016).
 25. Belo, D., Ribeiro, D. C., Pinho, P. & Carvalho, N. B. A Selective, Tracking, and Power Adaptive Far-Field Wireless Power Transfer System. *IEEE Trans. Microw. Theory Tech.* **67**, 3856–3866 (2019).
 26. Perera, T. D. P., Jayakody, D. N. K., Sharma, S. K., Chatzinotas, S. & Li, J. Simultaneous Wireless Information and Power Transfer (SWIPT): Recent Advances and Future Challenges. *IEEE Commun. Surv. Tut.* **20**, 264–302 (2018).
 27. Zhang, J. D., Wu, W. & Fang, D. G. Dual-Band and Dual-Circularly Polarized Shared-Aperture Array Antennas With Single-Layer Substrate. *IEEE Trans. Antennas Propag.* **64**, 109–116 (2016).
 28. Gomez-Villanueva, R., Jardon-Aguilar, H. & Miranda, R. L. Y. State of the Art Methods for Low SAR Antenna Implementation. In *Proceedings of the Fourth European Conference on Antennas and Propagation* 1–4 (2010).
 29. *IEEE Standard for Safety Levels with Respect to Human Exposure to Radio Frequency Electromagnetic Fields, 3 kHz to 300 GHz*, (IEEE, 2006); <https://www.fcc.gov/general/cell-phones-and-specific-absorption-rate>.
 30. *MSP430F552x, MSP430F551x Mixed-Signal Microcontrollers*, (Texas Instruments, 2020); https://www.ti.com/lit/ds/symlink/msp430f5529.pdf?ts=1657594103210&ref_url=https%253A%252F%252Fwww.ti.com%252Fproduct%252FMSP430F5529.
 31. Huynh, N. V. et al. Ambient Backscatter Communications: A Contemporary Survey. *IEEE Commun. Surv. Tut.* **20**, 2889–2922 (2018).
 32. Kimionis, J. & Tentzeris, M. M. Pulse Shaping: The Missing Piece of Backscatter Radio and RFID. *IEEE Trans. Microw. Theory Tech.* **64**, 4774–4788 (2016).
 33. Rotenberg, S. A. et al. Efficient Rectifier for Wireless Power Transmission Systems. *IEEE Trans. Microw. Theory Tech.* **68**, 1921–1932 (2020).
 34. Bharadia, D., Joshi, K., Kotaru, M. & Katti, S. BackFi: High Throughput WiFi Backscatter. *Acm Sigcomm. Comp. Com.* **45**, 283–296 (2015).
 35. Ju, L. et al. Stretchable and Dynamically Tunable Attenuator Based on Graphene. *IEEE Trans. Microw. Theory Tech.* **70**, 2999–3008 (2022).
 36. Chen, H. et al. All-Fabric Flexible Frequency-Selective-Rasorber Based on Cutting-Transfer Patterning Method. *Adv. Mater. Interfaces* **9**, 2200651 (2022).
 37. *BAR64-02V Low signal distortion, surface mount RF PIN diode*, (Infineon, 2018); https://www.infineon.com/dgdl/Infineon-BAR64-02V-DS-v01_01-EN.pdf?filed=5546d462689a790c01690f0247ae38fc.
 38. *Surface-Mount Mixer and Detector Schottky Diodes*, (Skyworks, 2021); https://www.skyworksinc.com/-/media/SkyWorks/Documents/Products/201-300/Surface_Mount_Schottky_Diodes_200041AG.pdf.
 39. Xunming, D. Optimization of a-SiGe based triple, tandem and single-junction solar cells. In *Thirty-first IEEE Photovoltaic Specialists Conference* 1365–1370 (2005).

Acknowledgements

This work was supported by the National Science Funds for Distinguished Young Scientists under grant number 61925103, the Project for Jiangsu Specially Appointed Professor, National Natural Science Foundation of China (NSFC) 62101115, and the Fundamental Research Funds for the Central Universities 2242022k60004.

Author contributions

J.-L. Z., W.-B. L. and T.-J. C. conceived and designed the research; J.-L. Z., C. D. and B.-Y. Y. designed the hardware. J.-L. Z. assembled and simulated EM performance. C. D., Z. S. and X.-H. L. wrote the software code. J. L., B.-Y. Y. and H. C. prepared the materials and performed the related characterizations. J.-L. Z. and H. C. performed general measurements and electromagnetic measurements of the hardware. C. D., J.-L. Z., X.-H. L. and Z.-M. C performed communication performance experiments. J.-L. Z. and C. D. analyzed the data. J.-L. Z., W.-B. L., C.D., B.-Y. Y., Z.-G. L., Y.-H. J. and T.-J. C. wrote the manuscript. All the authors discussed the results and commented on the manuscript.

Competing interests

The authors declare that they have no known competing financial interests or personal relationships that could have appeared to influence the work reported in this paper.

Additional information

Supplementary information The online version contains supplementary material available at <https://doi.org/10.1038/s41528-024-00304-4>.

Correspondence and requests for materials should be addressed to Wei-Bing Lu or Tie-Jun Cui.

Reprints and permissions information is available at <http://www.nature.com/reprints>

Publisher's note Springer Nature remains neutral with regard to jurisdictional claims in published maps and institutional affiliations.

Open Access This article is licensed under a Creative Commons Attribution 4.0 International License, which permits use, sharing, adaptation, distribution and reproduction in any medium or format, as long as you give appropriate credit to the original author(s) and the source, provide a link to the Creative Commons licence, and indicate if changes were made. The images or other third party material in this article are included in the article's Creative Commons licence, unless indicated otherwise in a credit line to the material. If material is not included in the article's Creative Commons licence and your intended use is not permitted by statutory regulation or exceeds the permitted use, you will need to obtain permission directly from the copyright holder. To view a copy of this licence, visit <http://creativecommons.org/licenses/by/4.0/>.

© The Author(s) 2024